Hindawi
Advances in Civil Engineering
Volume 2020, Article ID 8889606, 16 pages
https://doi.org/10.1155/2020/8889606

Research Article

Experimental Study on the Fracture Evolution Process of Rock-like Specimens Containing a Closed Rough Joint Based on 3D-Printing Technology

Jiawei Liu, Haijian Su, Hongwen Jing, Chengguo Hu, and Qian Yin

State Key Laboratory for Geomechanics and Deep Underground Engineering, China University of Mining and Technology, Xuzhou, Jiangsu 221116, China

Correspondence should be addressed to Haijian Su; hjsu@cumt.edu.cn

Received 24 June 2020; Revised 29 October 2020; Accepted 3 November 2020; Published 30 November 2020

Academic Editor: Fengqiang Gong

In order to overcome the disadvantage of traditional joint fabrication method—inability to reproduce the rough surfaces of practical rock joints—3D-printing technology was applied to restructure five kinds of rough joint according to the failure surface formed by the triaxial prepeak unloading test in this study. And uniaxial compression test was carried out on the rock-like specimens containing closed 3D-printing rough joint to study the effects of joint inclination and joint length on the mechanical properties (peak strength, peak strain, elastic modulus, and secant modulus), cracking process, and failure modes. Besides, digital image correlation (DIC) method and acoustic emission (AE) system are used to investigate the whole evolution process of strain fields and crack propagation during loading. It is found that the mechanical parameters decrease first and then go up as the joint inclination increases, while presenting a continuous downward trend with the increase of joint length. Inclination of 45° and the larger joint length bring more extensive reduction to mechanical properties of specimens. Specimens exhibit typical brittle failure characteristics. The failure mode of specimens affected by different joint inclination is tension-shear failure. And the joint scale rises; the failure mode of specimens changes from tensile failure to shear failure. Larger joint scale results in the longer prepeak fluctuation phase on axial stress-strain curves and more dispersed distribution of high-value AE counts.

1. Introduction

Natural rock, a complex geological medium, contains a great quantity of flaws (fissures, joints, holes, and weak surfaces) formed by a series of geological processes. The failure of rock under external loading is significantly affected by these pre-existing defects, from which the tensile cracks initiate [1–5]. Therefore, investigations on the fracture behaviors and related mechanical parameters of rock or rock-like specimen containing open or closed flaw play a significant role in ensuring the stability and security of practical rock engineering, such as underground engineering, dam base rock engineering, and high slope rock engineering, etc.

Many experimental works have been done to study the mechanical parameters, cracks initiation, propagation, and coalescence of pre-cracked specimens [6–10]. Zhu et al. [11] studied the variations in mechanical parameter and failure mode of sandstone specimens containing arc fissures based on the uniaxial compression experiments, which found that the degradation of the bearing capacity and the number of cracks that appear during the sandstone loading process decrease as the arc angle of the fissure increases. By combining numerical simulation and mechanical test results, the individual influence of three parameters (joint location, joint orientation, and trace length) on the compression strength of specimens has been explored by Xu et al. [12]. Wong and Einstein [13] identified seven types of cracks (three types of tensile cracks, three types of shear cracks, and a mixed tensile-shear crack) of tested gypsum and Carrara marble specimens under uniaxial compression based on their geometry and propagation mechanism. Uniaxial compression test was also carried out on the cuboid sandstone specimens containing single open fissure to investigate the effects of fissure angle and length on mechanical parameters and AE

behaviors of sandstone specimens by Yang and Jing [14], in which the other two types of cracks (lateral crack and far-field crack) were pointed out. The effects of the combination of a single hole and an inclined fissure on the sandstone specimens were investigated by Yin et al. [15], in which a high-speed camera was used to capture the whole deformation process so as to analyze the relation between axial stress-strain curve and the real-time crack coalescence.

In addition to the natural rock mentioned above, the rock-like materials, which have similar basic mechanical properties to real rock, have been widely used to explore the initiation, propagation, and coalescence behavior of cracks [16–22]. The gypsum specimens with three and sixteen flaws were made to investigate the crack coalescence under uniaxial compression by Sagong and Bobet [23], which pointed out that the wing cracks are in a stable manner, while secondary cracks are likely to exhibit unstable propagation. Ma et al. [24] studied the crack growth features of kinked fissures in the photosensitive resin material based on 3D-printing technology. The results showed that the tensile crack propagation of wing crack is the main cause of failure of the antisymmetric kinked crack. After the investigation on the compressive failure process of rock-like specimens containing two *X*-type flaws, Zhang et al. [25] found that the flaws tend to coalesce by cracks emanating from flaw tips along a potential path that is parallel to the maximum compressive stress direction. By comparing the experimental results of uniaxial compression test on the gypsum specimens with open and closed flaws, Park and Bobet [26] demonstrated the development manner and corresponding influencing factors of three types of cracks (wing cracks, coplanar cracks, and oblique secondary cracks). And significantly, it is concluded that the main difference between experimental results from open and closed flaws appears to be the quantity in the initiation stress, but not the fundamental fracture mechanisms and principles, which bridges the connection between the analyses on open flaws and closed flaws.

However, to sum up, the methods used in most related studies to prefabricate rock joints can be divided into two categories: (1) high-pressure hydraulic cutting and (2) insertion of mica, paper, and thin steel disc. An obvious disadvantage led by these conventional artificial methods is the inability to simulate the rough surfaces of practical rock joints. But with the development of industrial manufacturing, the combination of 3D scanning and 3D-printing technology is likely to be the great solution to this issue for its application on the replication of internal defects and fabrication on geological material [27, 28]. Furthermore, in the geotechnical field, by combination with the digital speckle correlation method (DSCM), the crack propagation evolution and the failure mode of tested specimens can be further explored [29]. Otherwise, glass, resin, barite, gypsum, and cement were commonly used in the previous fabrication of rock-like specimens [30–35]. But the use of resin or glass may lead to the loss of friction enhancement effect on the fracture surface compared to natural rock masses [36]. Though the mixture of the gypsum or ordinary cement and fine sand may achieve the friction effect, the limited bond strength of these specimens results in the difficulty in matching up the bearing capacity of real rocks and the relatively larger deformation under the action of external force. Therefore, in this study, high-strength Portland cement as well as the quartz powder was chosen to prepare the rock-like specimens. More significantly, based on the quantitative data obtained from the measurement towards the experimental failure surface of sandstone by three-dimensional scanning system, the rough joints were fabricated by the use of the 3D-printing technology. The fracture behaviors of rock-like material with closed 3D-printing rough joint with different joint inclinations and joint lengths under uniaxial compression were investigated.

2. Experimental Method

2.1. Properties of Sandstone Material. The sandstone material chosen for the experiments in this study was directly collected from the same working face in kilometer-depth Kouzidong coal mine, Anhui Province, China. The sandstone block was maintained with good integrity with no surface texture visible to naked eyes. According to the results of x-ray diffraction (XRD) (Figure 1(a)), the mineral compositions of tested sandstone mainly are quartz, feldspar, zeolite, and calcite. And by means of scanning electron microscope (SEM), it can be found that the chosen sandstone shows flat blocky crystalline structure under microscopic observation, as shown in Figure 1(b). Moreover, basic measurement and conventional triaxial compression test were conducted on the well-processed cylindrical sandstone specimens, to obtain the physical and mechanical properties of the sandstone, respectively. As shown in Table 1, the density, compressive strength, elastic modulus, tensile strength, cohesion, and internal friction angle of the sandstone specimens are 1.95 g/cm^3, 98.1 MPa, 13.5 GPa, 8.9 MPa, 31.58 MPa, and 27.33°, respectively.

2.2. Design and Preparation for the Rock-like Specimens Containing Closed 3D-Printing Rough Joint. The flow chart of the whole experimental program is shown in Figure 2.

To simulate the stress concentration and unloading effect during the process of excavation of underground engineering, the conventional triaxial prepeak unloading test was carried out with the confining pressure setting of 30 MPa on the well-processed cylindrical sandstone specimens to obtain the failure mode of specimen [37], as shown in Figure 3(a). Quantitative spatial coordinate data of the fracture plane was obtained by three-dimensional scanning system [38]. In order to ensure the accuracy, the spatial coordinate data was imported into the software MATLAB for surface fitting and 3D modeling (Figure 3(b)). A rectangular area 40.0 mm long and 30.0 mm wide was selected as research area (Figure 3(c)). A series of diminished areas with a fixed aspect ratio (4 : 3) within the research area were selected as prototypes for the rough joint fabrication (Figures 3(c)–3(g)). The above five kinds of 3D rough joint models were imported to a SLA660 3D printer with the high

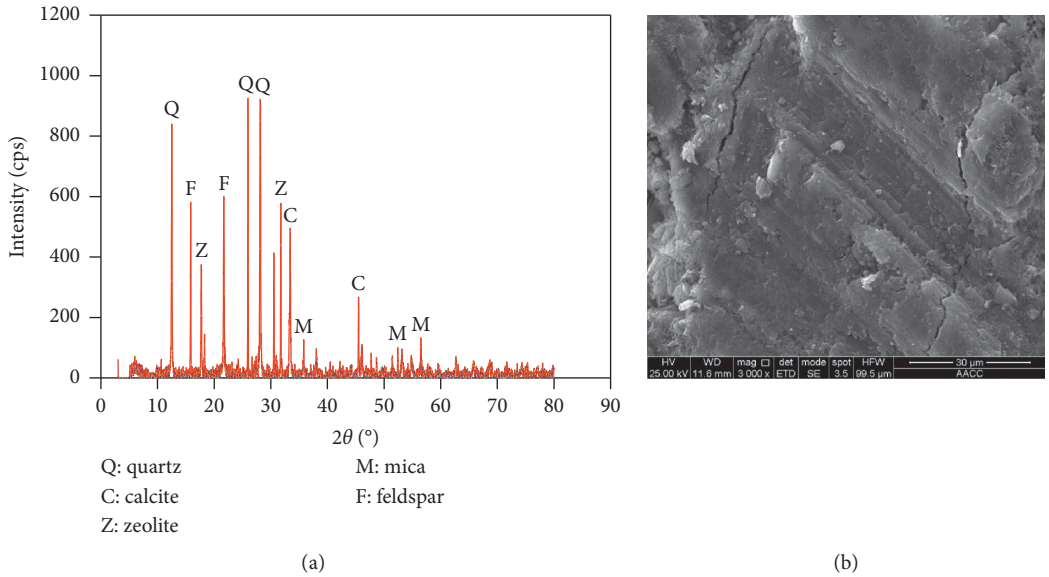

Figure 1: (a) XRD and (b) SEM results of sandstone in this research.

Table 1: Physical and mechanical parameters of sandstone and rock-like material.

	ρ (g/cm^3)	σ_c (MPa)	E_a (GPa)	σ_t (MPa)	c (MPa)	φ (°)
Sandstone	1.95	98.1	13.5	8.9	31.58	27.33
Rock-like material	2.07	100.3	11.8	6.8	30.11	23.87

Note: ρ indicates the density, σ_c indicates the compressive strength, E_a indicates the elastic modulus, σ_t indicates the tensile strength, c indicates the cohesion, and φ indicates the internal friction angle.

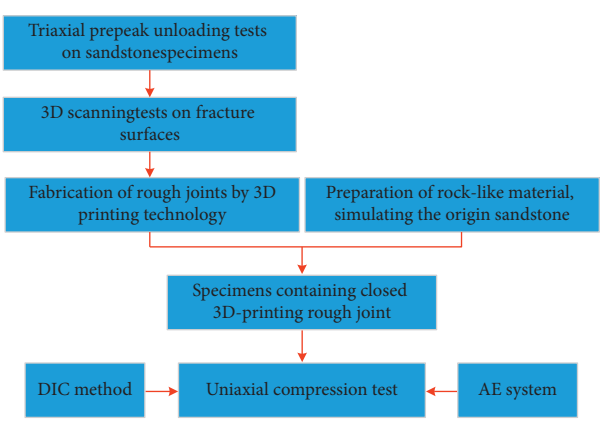

Figure 2: Test procedure.

printing accuracy of 0.05 mm. Under high-intensity laser irradiation, photosensitive resin, the raw material for 3D-printing, was shaped and solidified into a single-layer surface with the thickness of 0.05 mm. With the accumulation of surface layers, the complete 3D-printing rough joint with the thickness of 0.5 mm was finished.

To match up the hard brittleness of sandstone, high-strength Portland Cement (Type 62.5) supplied by Zhonglian Cement Co., Ltd. in Xuzhou, Jiangsu Province, China, was selected as the cementing material. Besides, the quartz powders purchased from Fuhong Mineral Products Co., Ltd. in Shanxi Province, China, with high hardness and chemical stability, were chosen as the main component to improve the properties of products. Specimens were made of cement, quartz powder, and water with a suitable volume mixture ratio of 1 : 0.8 : 0.35. The physical and mechanical parameters of rock-like material are presented in Table 1. The density, compressive strength, elastic modulus, tensile strength, cohesion, and internal friction angle of the rock-like specimens are 2.07 g/cm^3, 100.3 MPa, 11.8 GPa, 6.8 MPa, 30.11 MPa, and 23.87°, respectively, which are close to those of sandstone. As shown in Figure 4, samples are fabricated in the following steps. First, each 3D-printing rough joint was fixed inside a mold by four rigid filaments, one end of which was tied to a corner of joint and the other end was pulled out along the hole and fixed, as shown in Figures 4(a) and 4(b). Then, the cement pastes were prepared by pouring the weighed cement, quartz powder, and water into a container and stirring at 2000 rpm for 10 minutes under an electric blender. Next, after pouring the fresh pastes carefully into the molds, the whole system was vibrated to release residual air bubbles. Afterwards, specimens were placed for 24 hours and then demoulded and cured at a constant temperature of 20°C and humidness of 95% for 28 days in total. Finally, specimens were dried in natural state and polished smoothly.

As shown in Table 2, two set of specimens, a total of 16, were fabricated:

(1) From T30-1 to T90-2: specimens containing 3D-printing rough joints with the same fixed size of

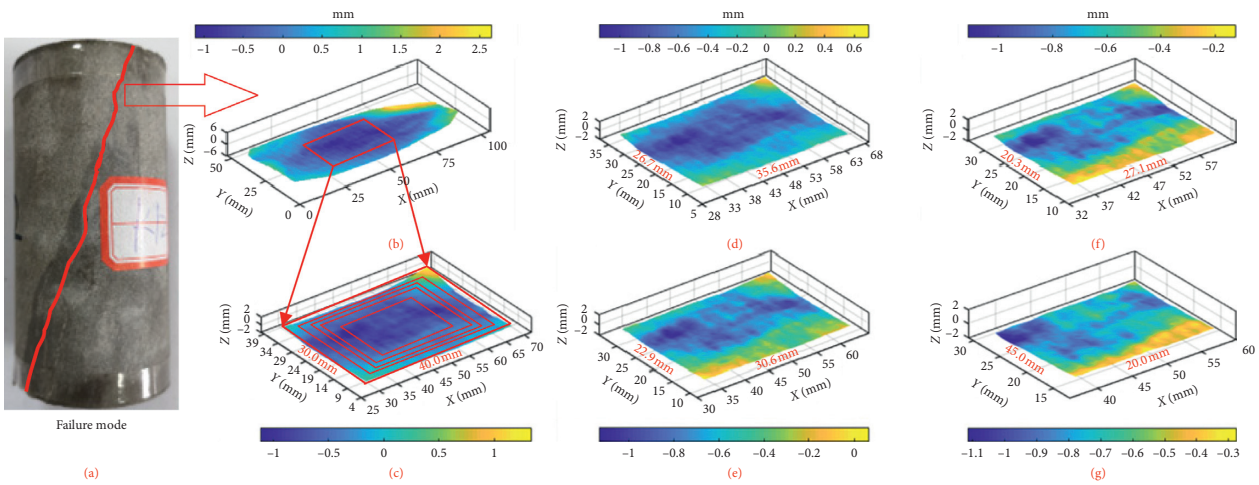

Figure 3: (a) Failure mode of sandstone specimen, (b) 3D image of fracture surface, (c) research area ($l = 40.0$ mm, $w = 30.0$ mm), (d) $l = 35.6$ mm, $w = 26.7$ mm, (e) $l = 30.6$ mm, $w = 22.9$ mm, (f) $l = 27.1$ mm, $w = 20.3$ mm, and (g) $l = 20.0$ mm, $w = 15.0$ mm.

40.0 mm × 30.0 mm, but different inclination angles, i.e., 30°, 45°, 60°, and 90°, were prepared to investigate the effects of joint inclinations on specimens.

(2) From S1-1 to S4-2: specimens containing 3D-printing rough joints with the same inclination angle of 60°, but different joint size, i.e., 35.6 mm × 26.7 mm, 30.6 mm × 22.9 mm, 27.1 mm × 20.3 mm, and 20.0 mm × 15.0 mm, were made to study the influences of joint lengths on specimens, as shown in Figures 3(d)–3(g).

2.3. Testing Procedure. The uniaxial compression test was carried out on all the specimens containing closed 3D-printing rough joint by using the MTS 816 rock mechanics servo-controlled testing system, as shown in Figure 5. The maximum loading capacity of the system was 1459 kN. The displacement-controlled mode with the loading rate of 2.5×10^{-3} mm/s was chosen in this test. Besides, an AE system was used to collect the internal signals of samples, and a digital photogrammetric system was used to monitor the strain variation of samples.

Before the test, the speckles were artificially fabricated on the specimens to improve the surface resolution of the specimens and facilitate the collection of experimental data. And the AE sensor was mounted on the specimens' surface to collect the acoustic signal in the testing process. Besides, a layer of Vaseline was coated evenly at both ends of specimens to reduce the friction between the end of the specimen and the indenter so as to ensure the accuracy of the test results. During the whole loading process, the axial load and displacement of the specimen were simultaneously recorded by the testing system. And, two high-definition cameras mounted on the same horizontal plane with a customized tripod were used to capture real-time photos for cylindrical testing specimens. In this way, the three-dimensional position was recovered according to the principle of the binocular stereovision technique [39]. After the test, the collected photos were analyzed by a DIC system to convert surface data into plane strain field so as to investigate the deformation behaviors of the specimens.

3. Experimental Results and Discussion

3.1. Uniaxial Stress-Strain Curves of Specimens with Different Rough Joint Geometries. Typical axial stress-strain curves for specimens containing rough joints with different joint inclinations and joint lengths under uniaxial compression are presented in Figure 6, from which it can be clearly seen that joint inclination and joint length have substantial impact on the strength and deformation behaviors of specimens under uniaxial compression. The axial stress of all tested specimens plunges to nearly zero after the peak stress, exhibiting typical brittle failure characteristics. The axial stress-strain curves of rock-like material specimens containing rough joint can be approximately divided into four states, i.e., compaction, elastic deformation, crack growth, and propagation and ultimate fracture. Next, the axial stress-strain curves of tested samples will be analyzed in detail from these four stages:

(1) Compaction: at this stage, axial stress-strain curves of specimens with different rough joint geometries present downward concaves, the axial stress increasing slower than the axial strain. These nonlinear behaviors are due to the fact that, at the very beginning of the test, the axial deformation of samples led by machine loading mainly results in the closure of some pre-existing micro-fissures and pores inside the specimens rather than the internal extrusion of ideal elastic continuum. Moreover, at this stage, all the axial stress-strain curves of samples are almost identical, meaning that the rigidity of samples has great consistency. And the different joint geometries have little effect on the mechanical properties of specimens in this stage.

(2) Elastic deformation: when higher loading level is applied to samples, the axial stress-strain curves of

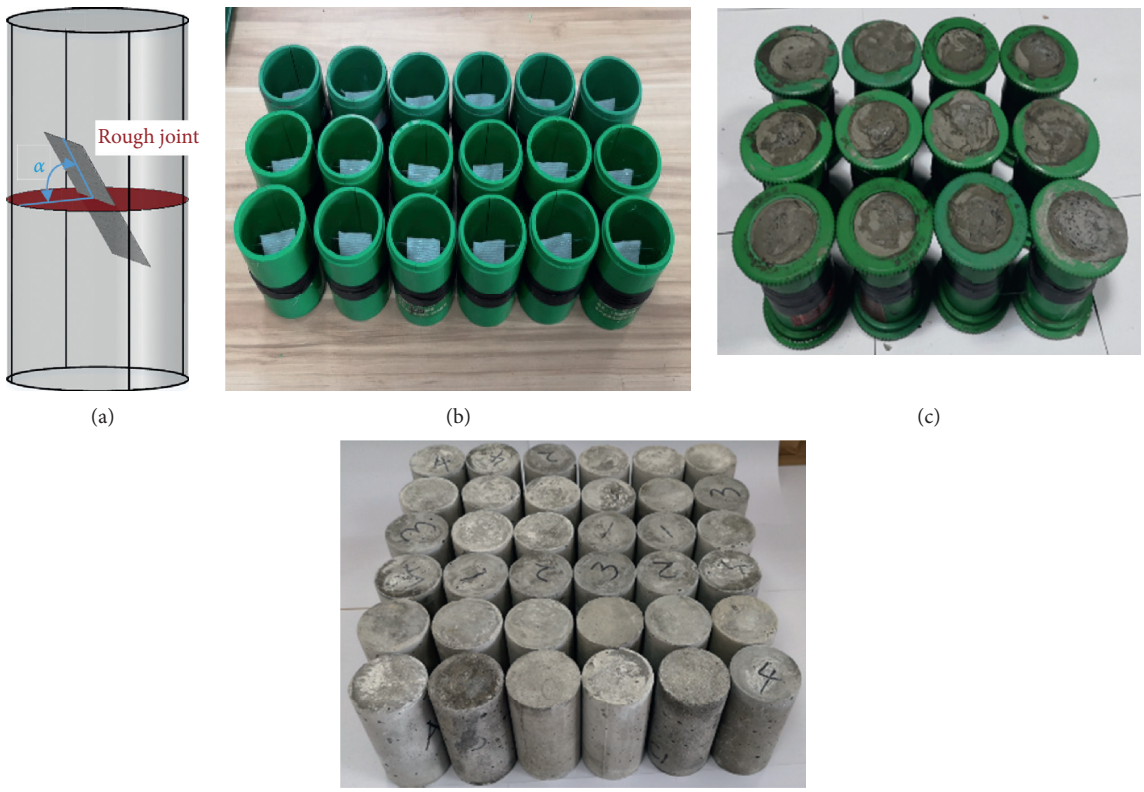

Figure 4: (a) Schematic diagram and (b) actual image of rough joint setting inside specimens, (c) specimens casting, and (d) finished products.

Table 2: Size and basic setup of specimens and closed rough joint.

No.	d (mm)	h (mm)	Inclination α (°)	Joint length l (mm)	Joint width w (mm)	w/l
T30-1	50.24	100.21	30	40.0	30.0	0.75
T30-2	50.37	100.10	30	40.0	30.0	0.75
T45-1	50.38	98.33	45	40.0	30.0	0.75
T45-2	50.58	98.83	45	40.0	30.0	0.75
T60-1	50.16	100.43	60	40.0	30.0	0.75
T60-2	50.50	100.23	60	40.0	30.0	0.75
T90-1	49.99	100.17	90	40.0	30.0	0.75
T90-2	50.32	99.73	90	40.0	30.0	0.75
S1-1	49.92	97.29	60	20.0	15.0	0.75
S1-2	50.44	100.74	60	20.0	15.0	0.75
S2-1	50.52	100.00	60	27.1	20.3	0.75
S2-2	50.40	98.92	60	27.1	20.3	0.75
S3-1	49.65	100.00	60	30.6	22.9	0.75
S3-2	50.32	98.56	60	30.6	22.9	0.75
S4-1	50.52	98.77	60	35.6	26.7	0.75
S4-2	50.49	97.42	60	35.6	26.7	0.75

d: diameter of specimen; h: height of specimen.

compacted specimens become linear, entering the stage of elastic deformation, in which the relation between axial stress and axial strain satisfies Hooke's law. However, unlike the compaction stage, the curves of specimens with different joint geometries begin to separate from each other and show various slopes, especially in Figure 6(a), demonstrating that the differences in inclination and length of rough joints begin to affect the stress-strain behaviors of specimens.

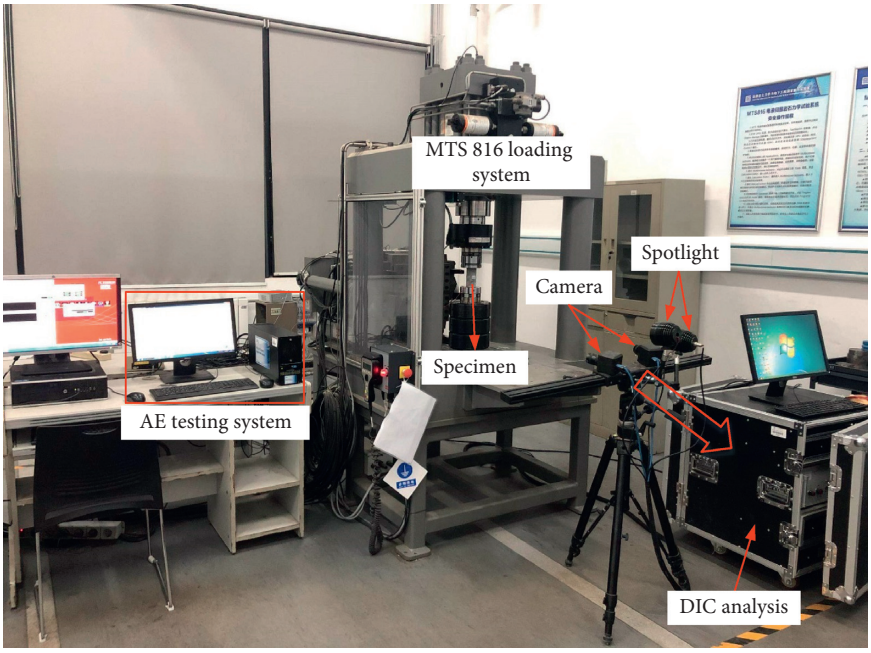

Figure 5: Testing system.

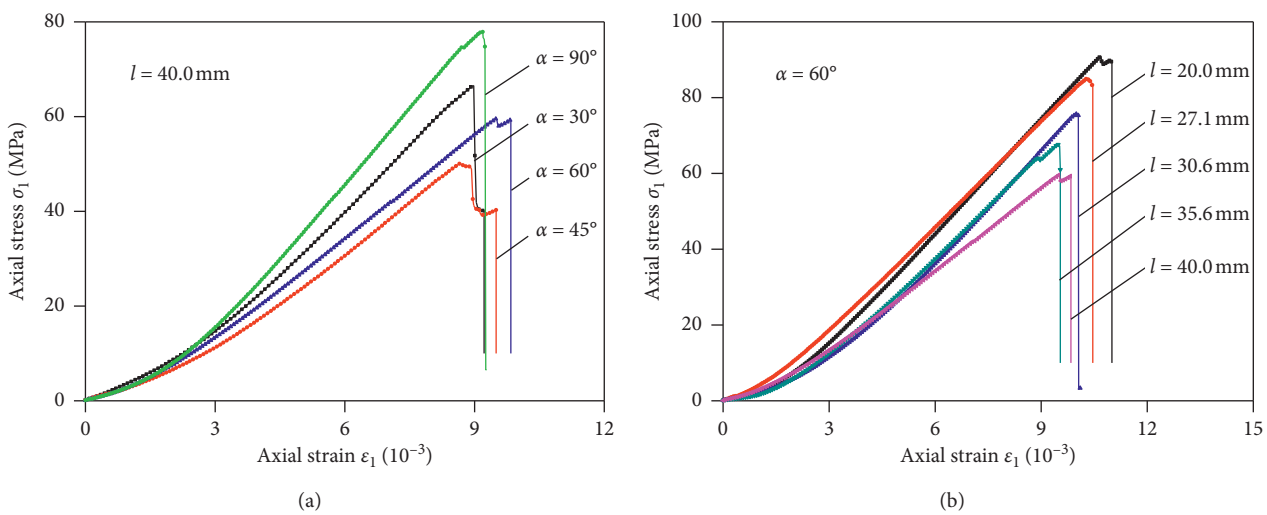

Figure 6: Stress-strain curves of specimens containing rough joint with different (a) joint inclinations and (b) joint lengths.

(3) Crack growth and propagation: in this stage, the axial stress-strain curves generally present nonlinear rising behavior with fluctuation. Stress level reaches the threshold of wing crack and even the secondary crack. Unlike the stable manner of wing tensile cracks, secondary cracks exhibit unstable propagation followed by the crack coalescence, resulting in the drop of axial stress, which can be clearly seen in the curves of sample $\alpha = 45^\circ$, sample $\alpha = 60^\circ$, sample $l = 20.0$ mm, and sample $l = 35.6$ mm. The development of cracks does not lead to the thorough fracture in this stage, which can be explained by the effective resistance structure formed by stress redistribution.

(4) Ultimate fracture: in this stage, macroscopic cracks come out, followed by the extensive surface spalling and brittle fracture, which leads to the plunge of axial stress to approximately 10 MPa, the residual stress.

3.2. Effect of Rough Joint Geometries on Mechanical Parameters of Specimens. The influence of inclination angle and length of rough joints on mechanical parameters of the specimens containing rough joint under uniaxial compression is shown in Figures 7 and 8, respectively. And the four mechanical parameters are, respectively, defined as follows. The σ_{1p} and ε_{1p} are described as the peak strength

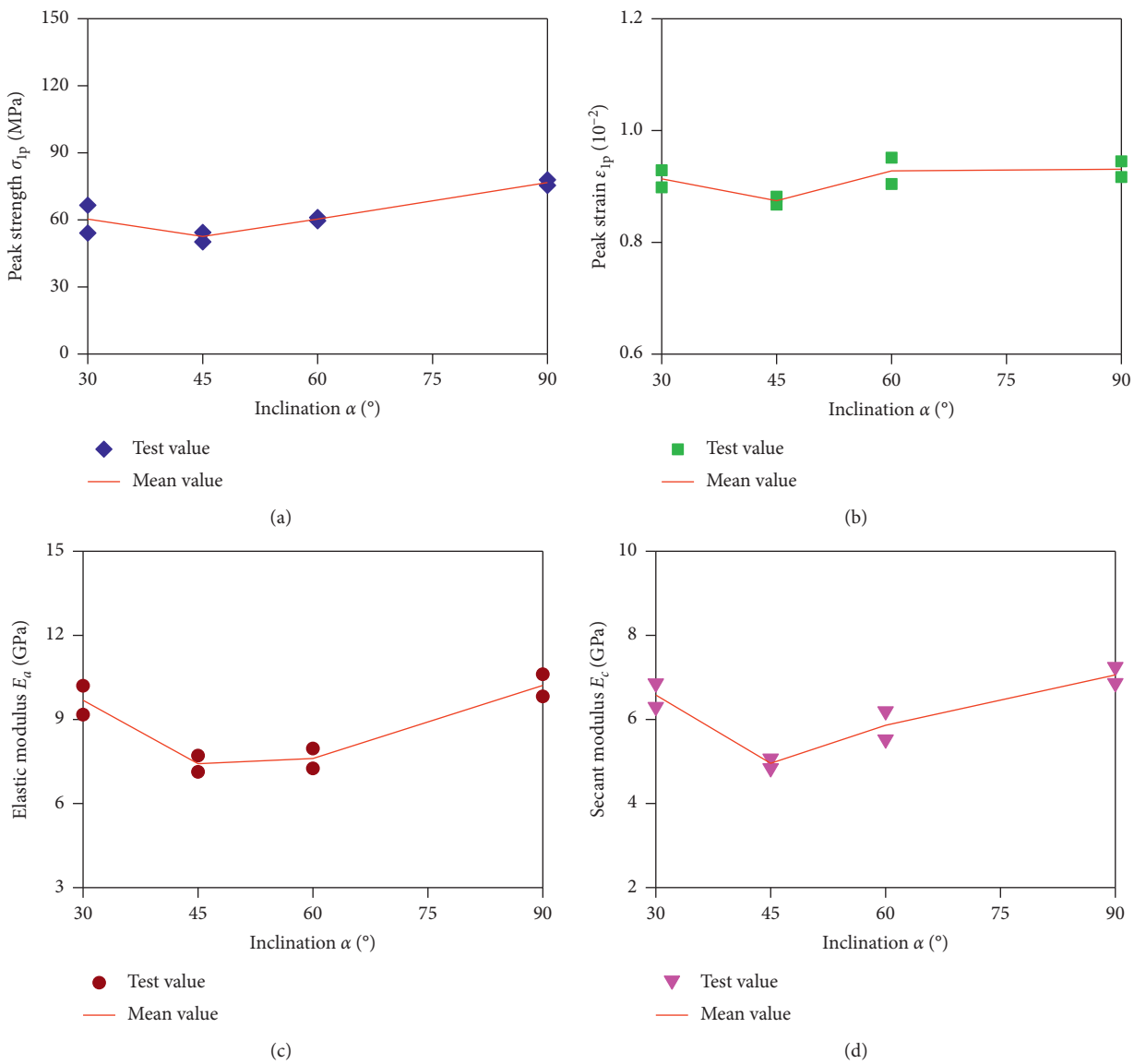

Figure 7: Effects of joint inclination on (a) peak strength, (b) peak strain, (c) elastic modulus, and (d) secant modulus of specimens, respectively ($l = 40.0$ mm).

and peak strain, respectively. E_s and E_c represent the elastic modulus and secant modulus, respectively.

From Figures 7 and 8, it is clear that, with joint inclination increases, four mechanical parameters all experience a deterioration and then go up, while there is continuous negative correlation between joint length and mechanical parameters. As the inclination increases from 30° to 45°, peak strength, peak strain, elastic modulus, and secant modulus descend from 60.34 MPa, 0.91×10^{-2}, 9.68 GPa, and 6.57 GPa, to 52.58 MPa, 0.87×10^{-2}, 7.42 GPa, and 4.95 GPa, with the reduction extents of 12.8%, 4.3%, 23.3%, and 24.6%, respectively, reaching the bottom at the inclination angle of 45°. After that, from 45° to 90°, they rise to 76.68 MPa, 0.93×10^{-2}, 10.21 GPa, and 7.05 GPa, respectively, increased by 45.8%, 6.8%, 37.6%, and 42.4%. However, with the increasing joint length from 2.0 to 4.0 cm, peak strength, peak strain, elastic modulus, and secant modulus generally experience the trend of continuous decline from 89.53 MPa, 1.05×10^{-2}, 9.97 GPa, and 7.64 GPa, to 60.33 MPa, 0.92×10^{-2}, 7.60 GPa, and 5.87 GPa, with the reduction extents of 32.6%, 12.3%, 23.7%, and 23.1%, respectively.

From the analysis above, it can be concluded that 45° inclination and larger length of rough joints brings more extensive reduction to four mechanical parameters of specimens. Moreover, among all the inclination angles tested, samples with inclination angle of 90° exhibit the best mechanical behaviors, which may result from the great situation of crack growth and propagation. Remarkably, according to Figures 7(c) and 8(c), elastic modulus of samples changes a lot versus the inclination of rough joint, while there is an obvious stable state on the elastic modulus from $l = 2.00$ cm to $l = 3.56$ cm, with little reduction, which indicates that the joint inclination has more significant impact than joint size on the elastic deformation state of samples.

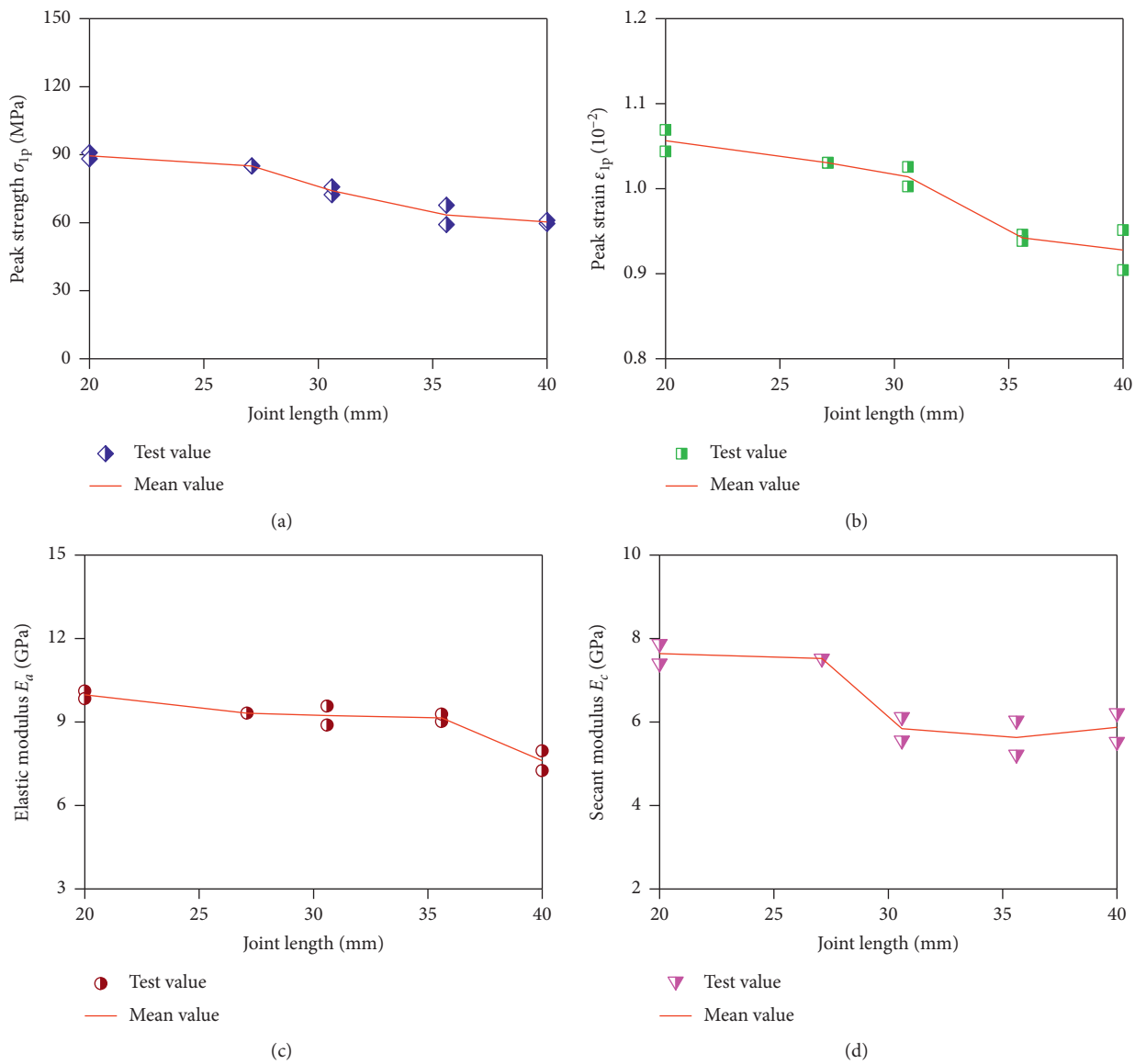

Figure 8: Effects of joint length on (a) peak strength, (b) peak strain, (c) elastic modulus, and (d) secant modulus of specimens, respectively ($\alpha = 60^{\circ}$).

In general, the change in joint length will lead to the differences in joint roughness. Three parameters, i.e., asperity's height, slope angle, and aspect, can be used to determine and visualize the three-dimensional joint roughness degree under different normal stresses and shear displacements [38]. Here, the three-dimensional surface of the fracture surface was discretized into a series of mesoscopic planes to analyze. Asperity's height represents the height with respect to the surface average height. The plane inclination angle with respect to the horizontal plane is defined as slope angle. And the aspect can be described as the angle between the projection of the normal vector of mesoscopic plane on horizontal plane and the north direction. Figure 9 presents the standard deviations (StDev) of asperity's height, slope angle, and aspect. With the rise of joint length, StDev of asperity's height and slope angle exhibit similar rising trend with increasing growth rate, while the StDev of slope increases with decreasing growth rate. Three exponential functions were used to make a great description to the connection between joint roughness coefficients and joint length, with the fitting coefficient R^2 ranging from 0.9246 to 0.9885.

3.3. Evolution Process of Specimens Containing Closed 3D-Printing Rough Joint

3.3.1. Strain Field and AE Behaviors of Specimens with Different Joint Inclinations. The strain field results of specimens containing closed 3D-printing rough joint with different joint inclinations are presented in Figure 10. Totally, five moments when the loading levels, respectively, reach $10\%\sigma_{1p}$, $40\%\sigma_{1p}$, $80\%\sigma_{1p}$, $95\%\sigma_{1p}$, and σ_{1p} are investigated for each specimen. In general, specimens with

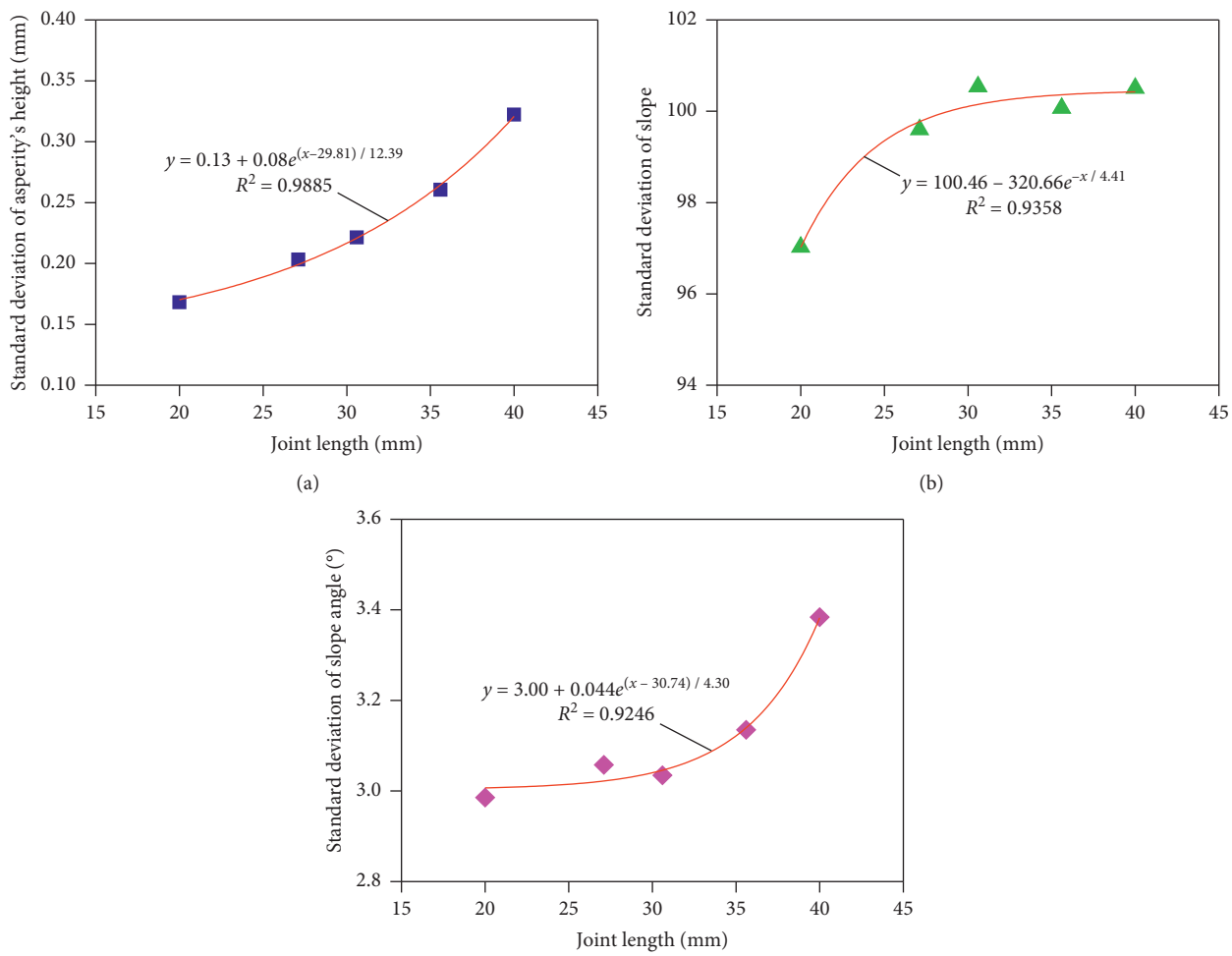

Figure 9: Relations between joint length and standard deviations of (a) asperity's height, (b) slope, and (c) aspect, respectively.

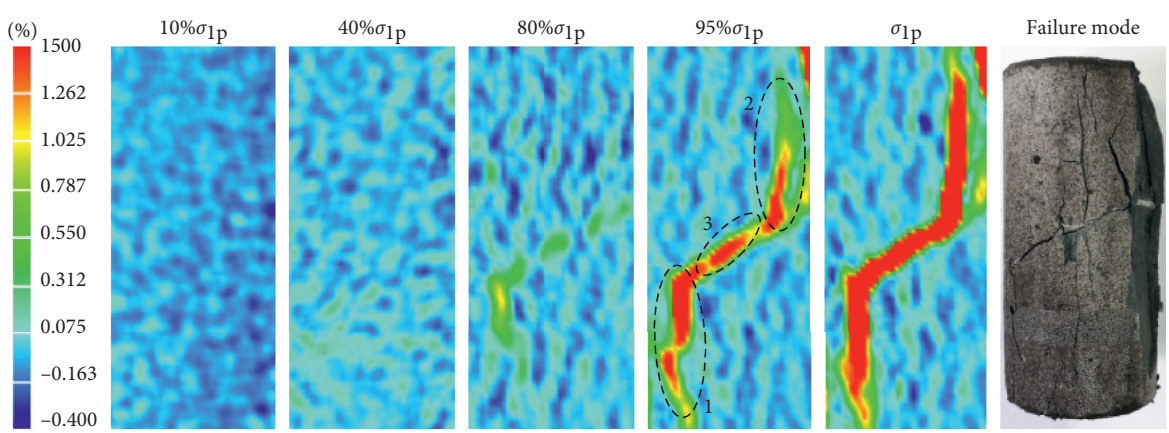

(a)

Figure 10: Continued.

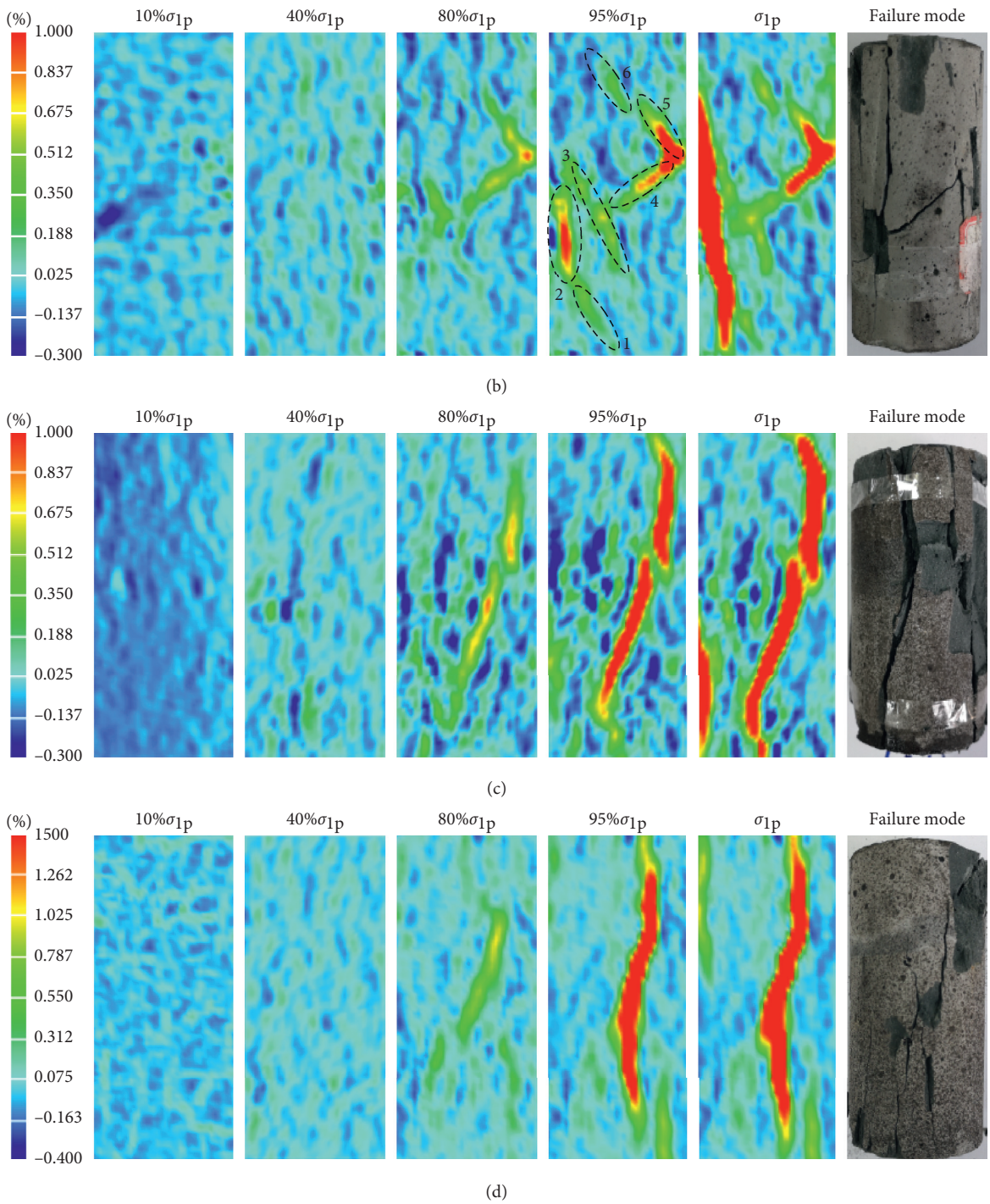

Figure 10: Evolution process of strain fields of specimens containing closed 3D-printing rough joints with different joint inclinations under uniaxial compression ($l = 40.0$ mm). (a) Specimen T30-2# ($\alpha = 30^\circ$), (b) specimen T45-2# ($\alpha = 45^\circ$), (c) specimen T60-2# ($\alpha = 60^\circ$), and (d) specimen T90-1# ($\alpha = 90^\circ$).

different joint inclinations exhibit brittle failure characteristics. At the low stress level of 10%σ_{1p} and 40%σ_{1p}, strain is very small with a relative random distribution. The variations on strain fields reflect the stress redistribution, which enables specimens to maintain structural stability with increasing stress. When the stress level reaches 80%σ_{1p}, the slit-shaped green areas with large strain values appear, which indicates the occurrence of obvious weak zones or even the microcracks on the surface of specimens. When the axial stress increases to 95%σ_{1p}, these areas turn red with larger size. It means that cracks propagate and coalesce, and finally the fully developed macrocracks are formed, followed by the ultimate fracture of specimens.

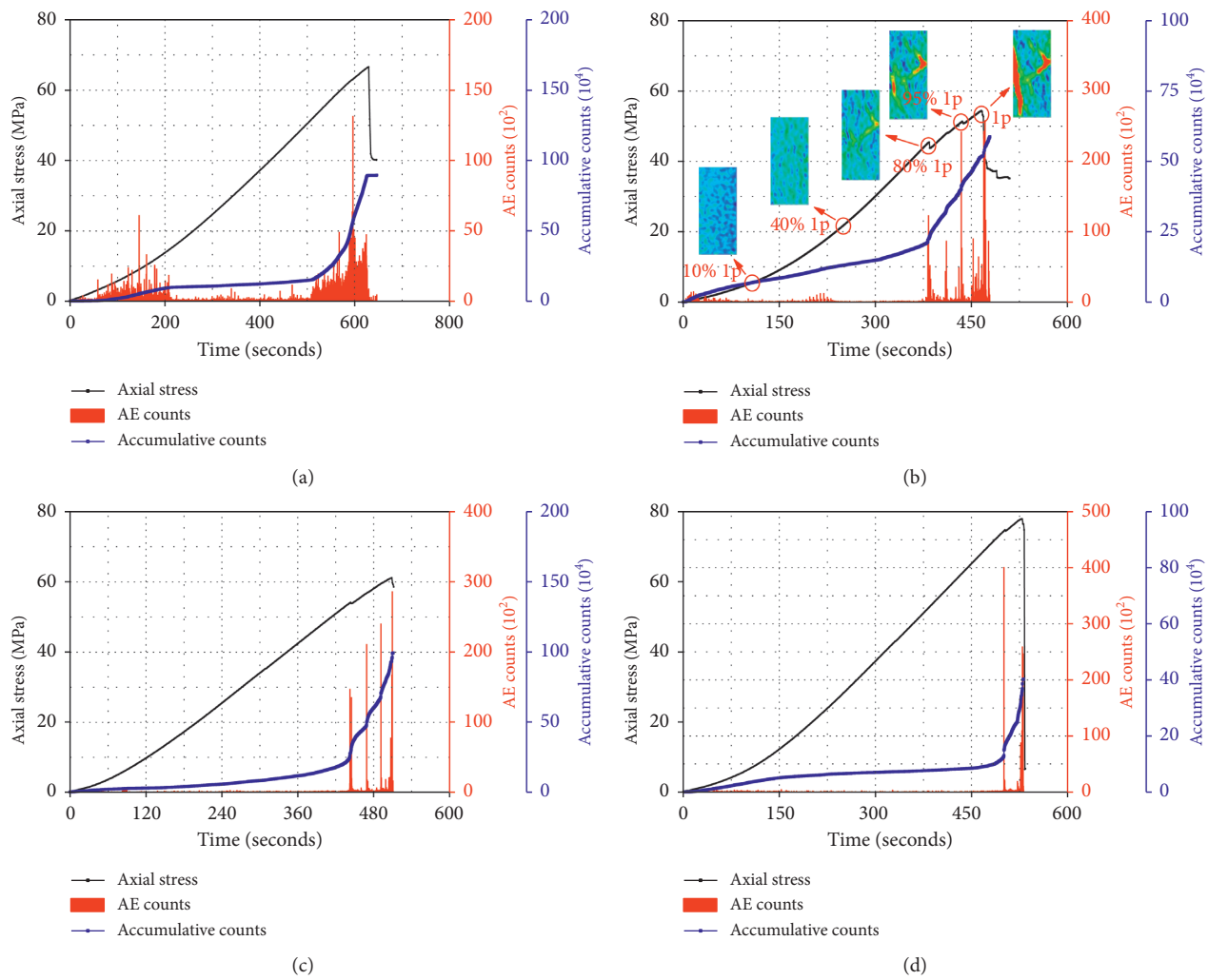

Figure 11: AE curves of specimens containing rough joint with different joint inclinations, i.e., (a) specimen T30-2# ($\alpha = 30^\circ$, $l = 40.0$ mm), (b) specimen T45-2# ($\alpha = 45^\circ$, $l = 40.0$ mm), (c) specimen T60-2# ($\alpha = 60^\circ$, $l = 40.0$ mm), and (d) specimen T90-1# ($\alpha = 90^\circ$, $l = 40.0$ mm) under uniaxial compression.

Crack characteristic is a great way to understand the failure mode of specimens [13, 14, 40, 41]. As the joint inclination increases from 30° to 90°, both tensile crack and shear crack can be found on the surface of specimens. For the specimen T30-2# ($\alpha = 30^\circ$), Positions 1 and 2 marked by the black circles in Figure 10(a) are typical tensile cracks. It can be clearly seen that, after initiating at the stress level of $80\%\sigma_{1p}$, the tensile crack continuously propagates along the direction of maximum compression. The position parallel to the stress direction and the stable expansion manner make the tensile crack not cause sudden and serious deterioration of the compression strength of the specimen [26]. Its coalescence with the shear crack (Position 3) and the form of through crack make the specimen finally loss its bearing capacity thoroughly. Specimens T60-2# ($\alpha = 60^\circ$) and T90-1# ($\alpha = 90^\circ$) have the similar tension-shear failure mode with specimen T30-2# ($\alpha = 30^\circ$). It is worth mentioning that specimen T45-2# ($\alpha = 45^\circ$) has obviously more complex stress state and distribution, compared to the specimens with other joint inclinations. At the stress level of $95\%\sigma_{1p}$, the number of slit-shaped stress concentration areas reaches six, two times that of specimen T30-2#. Besides, the inclination of 45° may make it easier to form more unstable shear zones and shear damage, resulting in serious decline of bearing capacity [42, 43]. This finding is consistent with the result of mechanical tests that the joint inclination of 45° makes the greatest reduction on the mechanical properties of rock-like specimens containing closed 3D-printing rough joint with different joint inclinations.

The AE behaviors of specimens affected by different joint inclinations of 3D-printing rough joint are shown in Figure 11. The AE behaviors can be approximately divided into two periods: quiet period and active period. At the quiet period, almost no large AE counts are collected and the accumulative counts present slow increase. By contrast, at the active period, several large values of AE counts appear along with the surge of accumulative counts. Take the specimen T45-2# ($\alpha = 45^\circ$, $l = 40.0$ mm) as an example; at the stress level of $10\%\sigma_{1p}$ and $40\%\sigma_{1p}$, during the compaction and crack propagation states, only little AE signal is collected

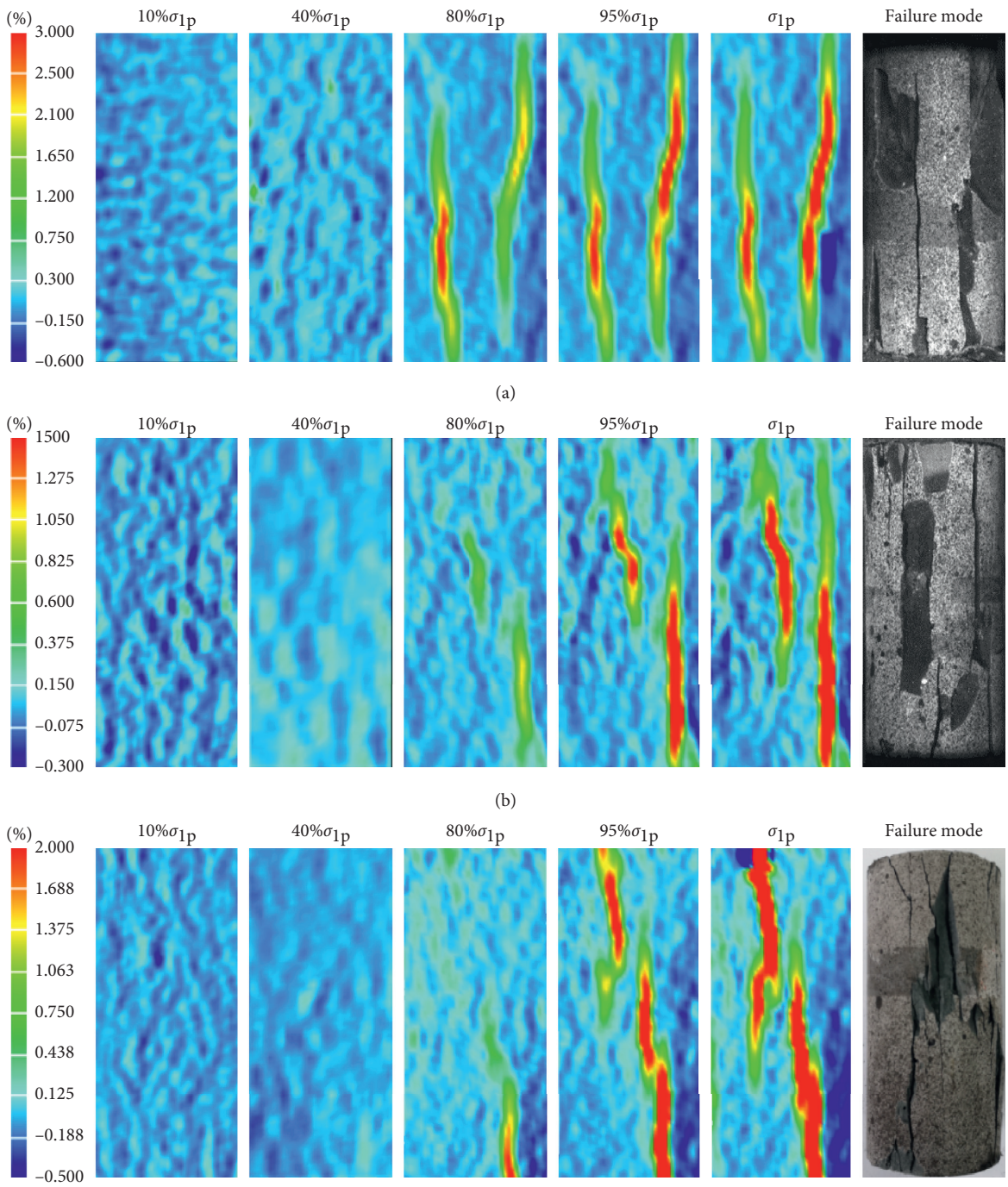

Figure 12: Continued.

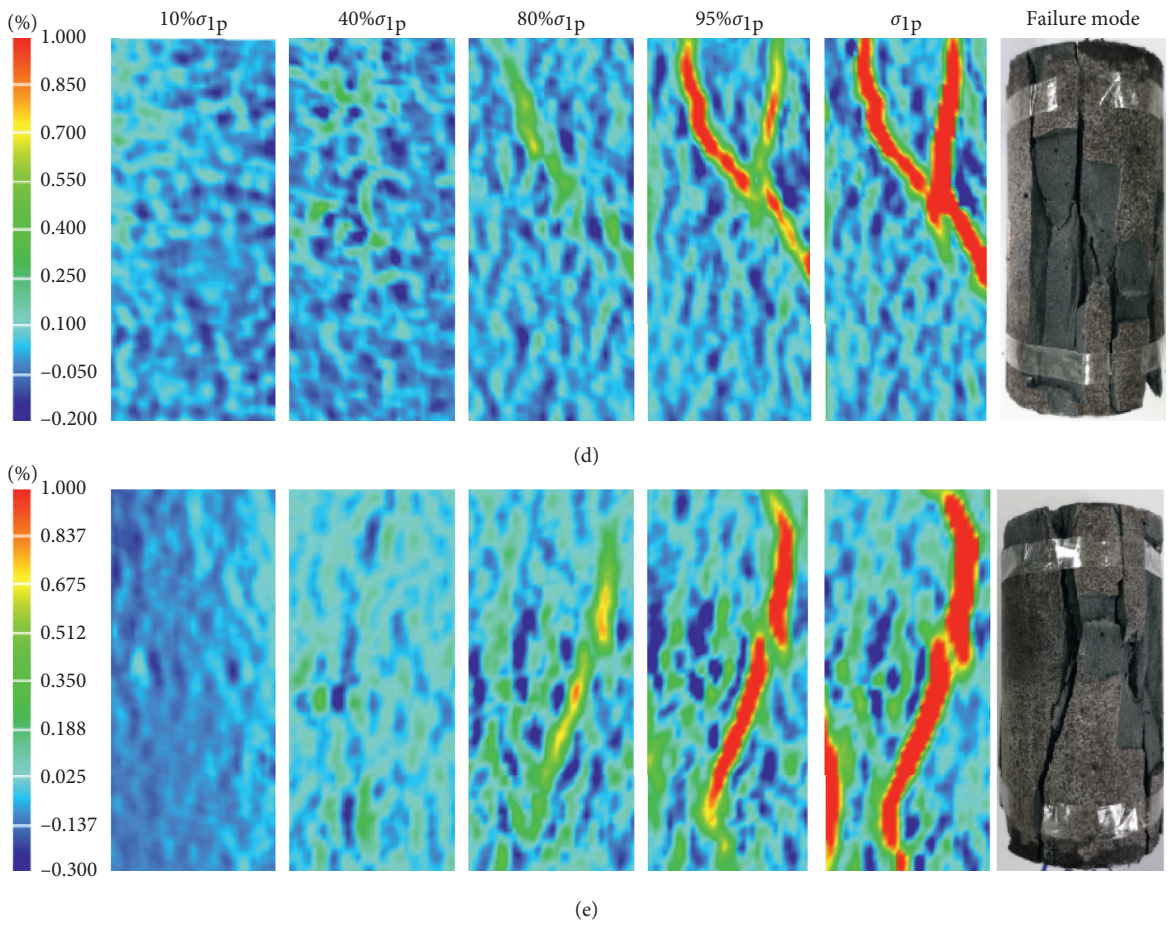

Figure 12: Evolution process of strain fields of specimens containing closed 3D-printing rough joints with different joint lengths under uniaxial compression ($\alpha = 60^{\circ}$). (a) Specimen S1-1# ($l = 20.0$ mm). (b) Specimen S2-1# ($l = 27.1$ mm). (c) Specimen S3-2# ($l = 30.6$ mm). (d) Specimen S4-1# ($l = 35.6$ mm). (e) Specimen T60-2# ($l = 40.0$ mm).

and the accumulative counts increase slowly. The AE behaviors stay in the quiet period. Correspondingly, no large strain area appears in the strain field at the stress level of $10\%\sigma_{1p}$ and $40\%\sigma_{1p}$. However, at the stress level between $80\%\sigma_{1p}$ and σ_{1p}, the AE enters the active period with a great amount of the large AE counts collected. The accumulative counts boost from 2.3×10^5 to 5.2×10^5 with the extent of 126%. Correspondingly, weak zones with large strain can be clearly seen in the strain fields of $80\%\sigma_{1p}$, $95\%\sigma_{1p}$, and σ_{1p}.

3.3.2. Strain Field and AE Behaviors of Specimens with Different Joint Scales. The variations on strain fields of specimens versus the joint length are shown in Figure 12. In general, specimens with different joint scales exhibit brittle failure characteristic. Until the strain values reach $80\%\sigma_{1p}$, the large strain areas appear, followed by the quick failure. As the joint length increases from 20.0 mm to 40.0 mm, the failure mode of specimens changes from tension failure to shear failure. When $l = 20.0$ mm (specimen S1−1#) and $l = 27.1$ mm (specimen S2−1#), the type of cracks is tensile crack. Tensile crack exhibits the propagation characteristics of extending to the upper and lower ends of the specimen, along the vertical direction (loading direction). There is no obvious crack coalescence on the surface of specimens. For specimen S3−2# ($l = 30.6$ mm), the far-field crack appears at the stress level of $80\%\sigma_{1p}$. When the stress level reaches $95\%\sigma_{1p}$ and σ_{1p}, the coalescence between tensile crack and far-field crack occurs on the surface of specimen. When $l = 35.6$ mm (specimen S4−1#) and $l = 40.0$ mm (specimen T60−2#), the shear cracks appear on the surface at $80\%\sigma_{1p}$ and then continue to propagate and coalesce until the ultimate failure. The change of failure mode from tension failure to shear failure may result from the decrease of effective bearing area caused by the increasing joint scale. And the unstable manner of shear crack leads to the greater deterioration of mechanical properties, which is consistent with the analysis in Section 3.2.

The AE behaviors of specimens containing rough joint with different joint lengths are displayed in Figure 13. It can be seen that, when the joint length is small from 20.0 mm to 30.6 mm (specimen S1−1#, specimen S2−1#, and specimen S3−2#), the prepeak fluctuation phase of axial stress-strain curves is relatively short, and correspondingly, the high AE counts are extremely concentrated. However, as the joint length increases to 35.6 mm and 40.0 mm (specimen S4−1# and specimen T60−2#), the prepeak fluctuation phase of axial stress-strain curves become longer, and the distribution of AE signals becomes dispersed. It can be explained by the findings from strain

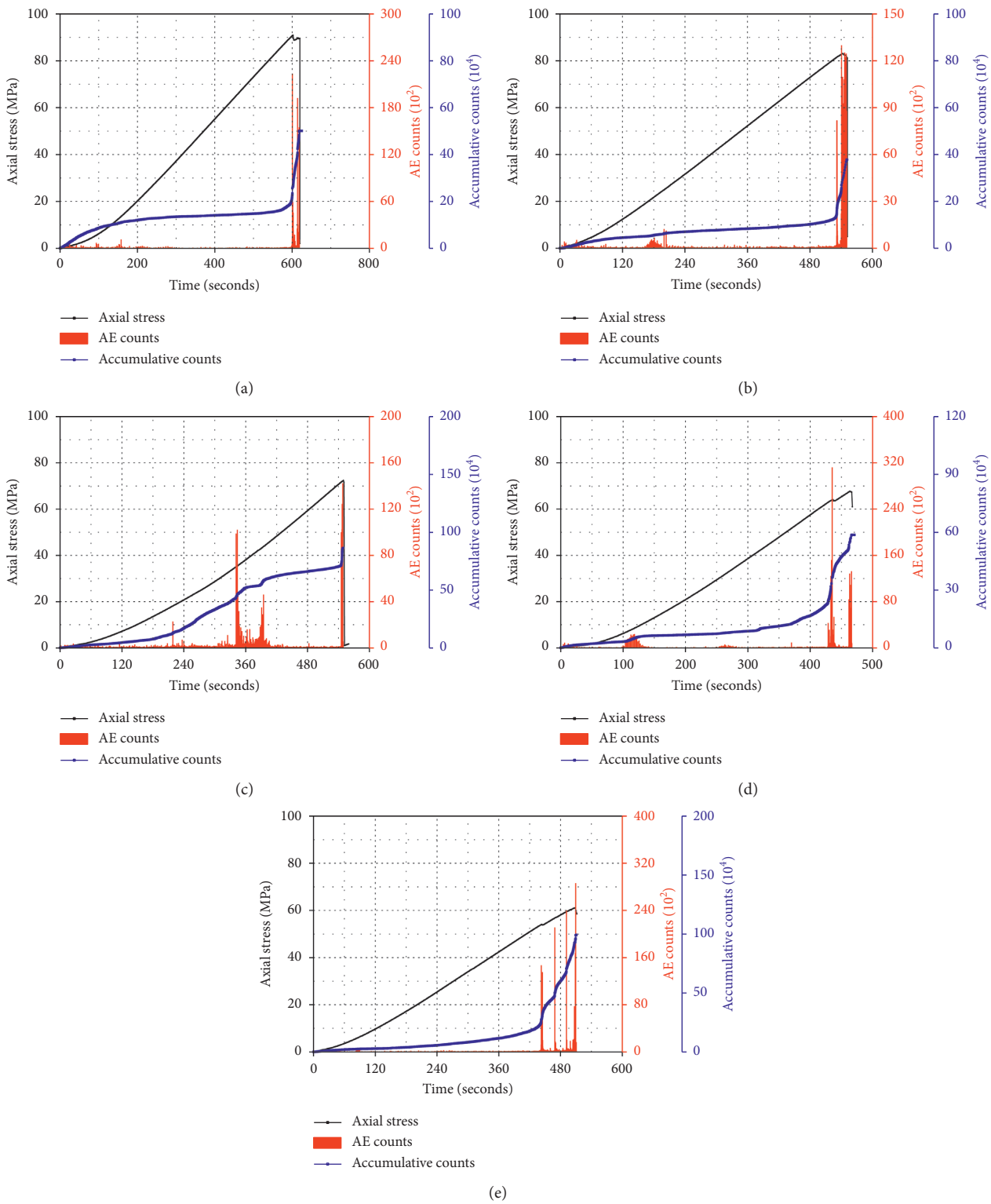

Figure 13: AE curves of specimens containing rough joint with different joint lengths, i.e., (a) specimen S1-1# ($l = 20.0$ mm, $\alpha = 60^\circ$), (b) specimen S2-1# ($l = 27.1$ mm, $\alpha = 60^\circ$), (c) specimen S3-2# ($l = 30.6$ mm, $\alpha = 60^\circ$), (d) specimen S4-1# ($l = 35.6$ mm, $\alpha = 60^\circ$), and (e) Specimen S5-2# ($l = 40.0$ mm, $\alpha = 60^\circ$) under uniaxial compression.

field and crack characteristic above. For specimens with small joint length (specimen S1−1#, specimen S2−1#, and specimen S3−2#), the types of crack are tensile crack and far-field crack. The expansion of these cracks is relatively stable, avoiding sudden and large deterioration of the bearing capacity of specimens. However, for specimens with large joint length

(specimen S4–1# and specimen T60–2#), the occurrence of shear cracks makes the active period of AE behaviors and prepeak fluctuation phase of axial stress-strain curves longer. It is worth noting that, for specimen S3–2#, the high AE counts collected at around 360s may result from the coalescence of tensile crack and far-field crack inside the specimen.

4. Conclusions

The uniaxial compression test was carried out on rock-like specimens containing closed 3D-printing rough joint with different joint inclinations and joint scales. Meanwhile, DIC method and AE system are applied to monitor and analyze the strain fields and AE behaviors of specimens, respectively. The main conclusions are obtained, as follows:

(1) Joint inclination and joint scale have a significant impact on the mechanical properties of rock-like specimens containing closed 3D-printing rough joint. As inclination increases from 30° to 90°, peak strength, peak strain, elastic modulus, and secant modulus all present decreasing trend first and then increase, reaching the bottom at inclination of 45°. Otherwise, when joint length rises from 20.0 mm to 40.0 mm, all these four mechanical parameters exhibit continuous decline. The inclination of 45° and larger joint scale bring more extensive reduction to the mechanical properties.

(2) As the joint inclination increases from 30° to 90°, the main failure mode of specimens is tension-shear failure. The joint inclination of 45° leads to more complicated stress state and internal shear slip, further resulting in a significant decrease in mechanical properties.

(3) When the joint scale increases from 20.0 mm to 40.0 mm, the failure mode of specimens changes from tensile failure to shear failure. Larger joint scale results in the longer prepeak fluctuation phase on axial stress-strain curves and more dispersed distribution of high-value AE counts.

(4) In addition to the joint inclination and joint scale, joint roughness coefficient (JRC) of the 3D-printing rough joint may also have an impact on the mechanical properties and failure mode of specimens. And the shear damage is a great point that can be used in the analysis on failure characteristics. These will be investigated in detail in the future study.

Data Availability

The original data used to support the findings of this study are available from the corresponding author (hjsu@cumt.edu.cn) upon request.

Conflicts of Interest

The authors declare that they have no conflicts of interest.

Acknowledgments

This study was financed by the National Natural Science Foundation of China (Nos. 42077240, 51704279, 51904290, and 51734009) and the Natural Science Foundation of Jiangsu Province of China (No. BK20170270).

References

[1] A. Bobet, "The initiation of secondary cracks in compression," *Engineering Fracture Mechanics*, vol. 66, no. 2, pp. 187–219, 2000.

[2] Y. P. Li, L. Z. Chen, and Y. H. Wang, "Experimental research on pre-cracked marble under compression," *International Journal of Solids and Structures*, vol. 42, no. 9-10, pp. 2505–2516, 2005.

[3] R. H. C. Wong, C. A. Tang, K. T. Chau, and P. Lin, "Splitting failure in brittle rocks containing pre-existing flaws under uniaxial compression," *Engineering Fracture Mechanics*, vol. 69, no. 17, pp. 1853–1871, 2002.

[4] H. Haeri, K. Shahriar, M. F. Marji, and P. Moarefvand, "On the strength and crack propagation process of the pre-cracked rock-like specimens under uniaxial compression," *Strength of Materials*, vol. 46, no. 1, pp. 140–152, 2014.

[5] S. Q. Yang, Y. H. Dai, L. J. Han, and Z. Q. Jin, "Experimental study on mechanical behavior of brittle marble samples containing different flaws under uniaxial compression," *Engineering Fracture Mechanics*, vol. 76, no. 12, pp. 1833–1845, 2009.

[6] P. S. Steif, "Crack extension under compressive loading," *Engineering Fracture Mechanics*, vol. 20, no. 3, pp. 463–473, 1984.

[7] Y.-H. Huang and S.-Q. Yang, "Mechanical and cracking behavior of granite containing two coplanar flaws under conventional triaxial compression," *International Journal of Damage Mechanics*, vol. 28, no. 4, pp. 590–610, 2019.

[8] H. Lee and S. Jeon, "An experimental and numerical study of fracture coalescence in pre-cracked specimens under uniaxial compression," *International Journal of Solids and Structures*, vol. 48, no. 6, pp. 979–999, 2011.

[9] A. M. Ferrero, M. Migliazza, R. Roncella, and G. Tebaldi, "Analysis of the failure mechanisms of a weak rock through photogrammetrical measurements by 2D and 3D visions," *Engineering Fracture Mechanics*, vol. 75, no. 3-4, pp. 652–663, 2008.

[10] S.-Q. Yang, Y.-H. Huang, P. G. Ranjith, Y.-Y. Jiao, and J. Ji, "Discrete element modeling on the crack evolution behavior of brittle sandstone containing three fissures under uniaxial compression," *Acta Mechanica Sinica*, vol. 31, no. 6, pp. 871–889, 2015.

[11] D. Zhu, H. W. Jing, Q. Yin, Y. J. Zong, and X. L. Tao, "Experimental study on mechanical characteristics of sandstone containing arc fissures," *Arabian Journal of Geosciences*, vol. 11, no. 20, Article ID 637, 2018.

[12] T. Xu, P. G. Ranjith, P. L. P. Wasantha, J. Zhao, C. A. Tang, and W. C. Zhu, "Influence of the geometry of partially-spanning joints on mechanical properties of rock in uniaxial compression," *Engineering Geology*, vol. 167, pp. 134–147, 2013.

[13] L. N. Y. Wong and H. H. Einstein, "Systematic evaluation of cracking behavior in specimens containing single flaws under uniaxial compression," *International Journal of Rock Mechanics and Mining Sciences*, vol. 46, no. 2, pp. 239–249, 2009.

[14] S.-Q. Yang and H.-W. Jing, "Strength failure and crack coalescence behavior of brittle sandstone samples containing a single fissure under uniaxial compression," *International Journal of Fracture*, vol. 168, no. 2, pp. 227–250, 2011.

[15] Q. Yin, H.-W. Jing, and T.-T. Zhu, "Experimental study on mechanical properties and cracking behavior of pre-cracked sandstone specimens under uniaxial compression," *Indian Geotechnical Journal*, vol. 47, no. 3, pp. 265–279, 2016.

[16] M. M. Kou, X. R. Liu, S. D. Tang, and Y. T. Wang, "3-D X-ray computed tomography on failure characteristics of rock-like materials under coupled hydro-mechanical loading," *Theoretical and Applied Fracture Mechanics*, vol. 104, Article ID 102396, 2019.

[17] P. Feng, F. Dai, Y. Liu, N. Xu, and P. Fan, "Effects of coupled static and dynamic strain rates on mechanical behaviors of rock-like specimens containing pre-existing fissures under uniaxial compression," *Canadian Geotechnical Journal*, vol. 55, no. 5, pp. 640–652, 2018.

[18] J.-W. Fu, S.-L. Liu, W.-S. Zhu, H. Zhou, and Z.-c. Sun, "Experiments on failure process of new rock-like specimens with two internal cracks under biaxial loading and the 3-D simulation," *Acta Geotechnica*, vol. 13, no. 4, pp. 853–867, 2018.

[19] S. Zhu, Z. H. Luo, Z. D. Zhu, Y. F. Gao, and N. Wu, "Construction of three-dimensional crack calculation method for transparent rock-like materials based on stereo vision principle," *Advances in Civil Engineering*, vol. 2019, Article ID 2021092, 13 pages, 2019.

[20] W. Yang, G. Li, P. Ranjith, and L. Fang, "An experimental study of mechanical behavior of brittle rock-like specimens with multi-non-persistent joints under uniaxial compression and damage analysis," *International Journal of Damage Mechanics*, vol. 28, no. 10, pp. 1490–1522, 2019.

[21] W. H. Tan and P. F. Wang, "Experimental study on seepage properties of jointed rock-like samples based on 3D printing techniques," *Advances in Civil Engineering*, vol. 2020, Article ID 9403968, 10 pages, 2020.

[22] T. L. Han, J. P. Shi, and Y. S. Chen, "Mechanical characteristics and failure characteristics of jointed rock under axial unloading and radial unloading," *Advances in Civil Engineering*, vol. 2020, Article ID 8812621, 15 pages, 2020.

[23] M. Sagong and A. Bobet, "Coalescence of multiple flaws in a rock-model material in uniaxial compression," *International Journal of Rock Mechanics and Mining Sciences*, vol. 39, no. 2, pp. 229–241, 2002.

[24] G. Ma, Q. Dong, and L. Wang, "Experimental investigation on the cracking behavior of 3D printed kinked fissure," *Science China Technological Sciences*, vol. 61, no. 12, pp. 1872–1881, 2018.

[25] B. Zhang, S. C. Li, X. Y. Yang et al., "The coalescence and strength of rock-like materials containing two aligned X-type flaws under uniaxial compression," *Geomechanics and Engineering*, vol. 17, no. 1, pp. 47–56, 2019.

[26] C. H. Park and A. Bobet, "Crack coalescence in specimens with open and closed flaws: a comparison," *International Journal of Rock Mechanics and Mining Sciences*, vol. 46, no. 5, pp. 819–829, 2009.

[27] W. L. Tian, S. Q. Yang, Z. L. Hu, and J. W. Lu, "Experimental study of the mechanical behavior of unfilled rough jointed specimens under uniaxial compression," *Arabian Journal of Geosciences*, vol. 13, Article ID 164, 2020.

[28] Q. Jiang, X. Feng, Y. Gong, L. Song, S. Ran, and J. Cui, "Reverse modelling of natural rock joints using 3D scanning and 3D printing," *Computers and Geotechnics*, vol. 73, pp. 210–220, 2016.

[29] L. Song, Q. Jiang, Y.-E. Shi et al., "Feasibility investigation of 3D printing technology for geotechnical physical models: study of tunnels," *Rock Mechanics and Rock Engineering*, vol. 51, no. 8, pp. 2617–2637, 2018.

[30] E. Hoek and Z. T. Bieniawski, "Brittle fracture propagation in rock under compression," *International Journal of Fracture*, vol. 1, no. 3, pp. 137–155, 1965.

[31] E. G. Bombolakis, "Photoelastic study of initial stages of brittle fracture in compression," *Tectonophysics*, vol. 6, no. 6, pp. 461–473, 1968.

[32] C. H. Park and A. Bobet, "Crack initiation, propagation and coalescence from frictional flaws in uniaxial compression," *Engineering Fracture Mechanics*, vol. 77, no. 14, pp. 2727–2748, 2010.

[33] L. N. Y. Wong and H. H. Einstein, "Crack coalescence in molded gypsum and carrara marble: part 2-microscopic observations and interpretation," *Rock Mechanics and Rock Engineering*, vol. 42, no. 3, pp. 513–545, 2009.

[34] J. Jin, P. Cao, Y. Chen, C. Pu, D. Mao, and X. Fan, "Influence of single flaw on the failure process and energy mechanics of rock-like material," *Computers and Geotechnics*, vol. 86, pp. 150–162, 2017.

[35] O. Mughieda and A. K. Alzo'ubi, "Fracture mechanisms of offset rock joints-a laboratory investigation," *Geotechnical and Geological Engineering*, vol. 22, no. 4, pp. 545–562, 2004.

[36] P. Cao, T. Liu, C. Pu, and H. Lin, "Crack propagation and coalescence of brittle rock-like specimens with pre-existing cracks in compression," *Engineering Geology*, vol. 187, pp. 113–121, 2015.

[37] D. Li, Z. Sun, T. Xie, X. Li, and P. G. Ranjith, "Energy evolution characteristics of hard rock during triaxial failure with different loading and unloading paths," *Engineering Geology*, vol. 228, pp. 270–281, 2017.

[38] M. Sharifzadeh, Y. Mitani, and T. Esaki, "Rock Joint Surfaces Measurement and analysis of aperture distribution under different normal and shear loading using GIS," *Rock Mechanics and Rock Engineering*, vol. 41, no. 2, pp. 299–323, 2008.

[39] Z. Z. Tang, J. Liang, Z. Z. Xiao, C. Guo, and H. Hu, "Three-dimensional digital image correlation system for deformation measurement in experimental mechanics," *Optical Engineering*, vol. 49, no. 10, Article ID 103601, 2010.

[40] R. H. Cao, P. Cao, H. Lin, X. Fang, C. Y. Zhang, and T. Y. Liu, "Crack initiation, propagation, and failure characteristics of jointed rock or rock-like specimens: a review," *Advances in Civil Engineering*, vol. 2019, Article ID 6975751, 31 pages, 2019.

[41] C. Wu, F. Gong, and Y. Luo, "A new quantitative method to identify the crack damage stress of rock using AE detection parameters," *Bulletin of Engineering Geology and the Environment*, 2020.

[42] E. Z. Lajtai, "Brittle fracture in compression," *International Journal of Fracture*, vol. 10, no. 4, pp. 525–536, 1974.

[43] Q. Jiang, B. Yang, F. Yan, C. Liu, Y. G. Shi, and L. F. Li, "New method for characterizing the shear damage of natural rock joint based on 3D engraving and 3D scanning," *International Journal of Geomechanics*, vol. 20, no. 2, pp. 1–15, 2020.